4D-CT lung motion estimation with deformable registration: Quantification of motion nonlinearity and hysteresis

Vlad Boldea[a)]
LIRIS Laboratory, Lyon 2 University, 5 av. P. Mendes-France, 69676 Bron, France and Radiotherapy Department, Leon Berard Cancer Center, 28 rue Laennec, 69008 Lyon, France

Gregory C. Sharp and Steve B. Jiang[b)]
Department of Radiation Oncology, Massachusetts General Hospital, 30 Fruit Street, Boston, Massachusetts 02114

David Sarrut
Radiotherapy Department, Leon Berard Cancer Center, 28 rue Laennec, 69008 Lyon, France and CREATIS Laboratory, INSA-Lyon, 7 av. Jean Capelle, 69621 Villeurbanne, France

(Received 31 July 2007; revised 13 November 2007; accepted for publication 3 January 2008; published 21 February 2008)

In this article, our goal is twofold. First, we propose and compare two methods which process deformable registration to estimate patient specific lung and tumor displacements and deformation during free breathing from four-dimensional computed tomography (4D-CT) data. Second, we propose techniques to quantify the physiological parameters of motion nonlinearity and hysteresis. A Fréchet distance-based criterion is introduced to measure the motion hysteresis. Experiments were conducted with 4D-CT data of five patients treated in radiotherapy for non-small cell lung cancer. The accuracy of deformation fields assessed against expert-selected landmarks was found to be within image voxel tolerance. The second method gave slightly better results in terms of accuracy and consistency, although the differences were not statistically significant between the two methods. Lung motion nonlinearity and hysteresis are patient specific, and vary across regions within the lung during respiration. For all patients, motion between end-exhale and end-inhale was well approximated with a straight line trajectory for the majority of lung points. Hysteresis was found to be globally correlated with trajectory length. The main limitation to the proposed method is that intensity-based deformable registration is dependent on image quality and image resolution. Another limitation is the absence of gold standard which makes the validation of the computed motion difficult. However, the proposed tools provide patient specific motion information which, in radiotherapy for example, can ease the definition of precise internal margins. In the future, the integration of physiological information from multiple patients could help to create a general lung atlas with different clinical applications. [DOI: 10.1118/1.2839103]

Key words: 4D-CT, lung, motion, deformable registration, hysteresis, nonlinearity

I. INTRODUCTION

Accurate motion modeling within the lung is an important consideration in different clinical applications. In lung cancer radiation therapy, for example, the motion is assessed for determination of planning margins[1] as well as four-dimensional (4D) optimization[2] and new delivery adaptations.[3] Respiratory motion has been modeled in a variety of ways for different purposes. The most common models use either phase, or amplitude, or both, and describe the motion of either a single point or a surrogate signal. A well known example is the cosine model of Lujan *et al.*,[4] in which motion is described by an analytic function of amplitude and phase. Other models include the average tumor trajectory,[5] the piecewise linear model,[6] and the five-dimensional (5D) motion model.[7]

More precise modeling of lung anatomy during breathing requires internal detail, which is now available mainly thanks to four-dimensional computed tomography (4D-CT)[8,9] or fast magnetic resonance imaging.[10–12] Variations of internal morphology over the free-breathing cycle can be observed thanks to these image modalities. Recent advances in multidetector-row CT scans make possible even the acquisition of functional and morphological information.[13] The 4D-CT images are among the solutions proposed to deal with respiratory movement in lung cancer radiotherapy. Four-dimensional-CT refers to a sequence of three-dimensional (3D)-CT images indexed by breathing state, acquired using retrospective sorting (based on respiration amplitude or phase) of fan-beam or cone-beam images, or by direct cine-mode acquisition with multi-slice geometries.[14,15]

In order to fully benefit from the information provided by 4D-CT, this data must be associated with new medical image analysis tools.[3,16] Sluimer *et al.*[17] give an interesting overview of image treatment and analysis techniques developed for CT scans. Among other tools, deformable image registration is an important topic with direct application to radiotherapy[18,16] because it allows to estimate organ defor-

mation and displacement. Several surveys provide a general overview of image registration theory and implementation.[19–21] In the present paper, the deformable registrations were computed with a method that we proposed in a previous work.[22] It is based on an optical flow method[23,24] with Gaussian regularization. To take into account lung intensity changes due to air variation during free breathing, we also proposed a pre-processing technique called a priori lung density modification (APLDM).[22] APLDM consists in changing lung intensities in the 3D-CT images of the 4D-CT in order to have lung intensity distributions similar to the end-exhale reference image.

The goal of this study is to propose patient specific motion computation methods allowing, first, to follow lung and tumor displacements and deformations along a free breathing cycle and, second, to extract physiological parameters like nonlinearity and hysteresis of lung motion. In radiotherapy, motion knowledge allows to automatically quantify tumor and organ motion, and would help to define personalized internal margins. This is an alternative to methods using fluoroscopy[25,26] to set appropriate internal margins, but based on 3D+t information instead of two-dimensional (2D)+t and on a single breathing cycle instead of several cycles. An accurate motion estimation could also help to build specific patient lung model which could be used to propose a reliable semiautomatic contour propagation tool in a 4D-CT image. It can also be used for dose computation at different breathing states, for dose distribution comparisons, or for helping to plan gated treatments. It may be also integrated in online image guidance procedures. In order to cope with any deviations from the 4D-CT derived motion trajectory or hysteresis during treatment, the model should be coupled with online monitoring: external markers (e.g., surface based sensors), or fluoroscopy, or any other online imagery solution (such as cone-beam CT, for example). The 4D-CT model alone could also be considered for patients with reproducible free breathing cycle, which is probably not the case for the majority of the patients. Another interesting application for such model is the simulation of dynamic ventilation images.[27]

I.A. Notations

This paragraph describes the principal notations used in the paper. The term *state* refers to a scalar parameterization of the geometry in time, phase, or amplitude. In 4D-CT data available for this study, the states correspond to discrete breathing phases. To each state X, $X \in \{0,1,2,\ldots,9\}$ corresponds an image of the geometry denoted I_X. In some cases we will refer to states that lie between the discrete states of the 4D-CT. This will be denoted by Φ or Ψ, with $\Phi, \Psi \in [X, X+1]$. A lung point in 3D will be denoted by $\mathbf{p}$, $\mathbf{p} \in \mathbb{R}^3$, and its position at state X (or Φ) will be denoted by $\mathbf{p}_X$ (or $\mathbf{p}_\Phi$). Given two different states X and Y of the 4D-CT, a vector field from X to Y is denoted by U_{XY}. The vector field describes the motion of each point $\mathbf{p}_X$ to its corresponding position $\mathbf{p}_Y$: $\mathbf{p}_Y = \mathbf{p}_X + U_{XY}(\mathbf{p}_X)$. A trajectory $T_\mathbf{p}$ describes the path followed by a single point $\mathbf{p}$ as it progresses through states from X to Y.

II. MATERIAL AND METHOD

In the first part of this study, we analyzed and compared two methods which process deformable registration to estimate lung motion from 4D-CT data. The first method computes small deformations estimated between neighboring phases, whereas the second method computes large deformations estimated between the end-exhale reference phase and all other phases. These two estimation methods were validated against ground truth (landmark points) and for internal consistency. In the second part of the study, we studied motion variations across the lung during the free-breathing cycle. Lung point trajectories were computed from deformation fields to assess motion nonlinearity and hysteresis. Such physiological information could be useful to decide if the motion between end-inhale and end-exhale could be approximated with a linear motion or if the non-linear motion is significative and should be taken into account, for example, for tumors with a motion hysteresis larger than their size. For hysteresis evaluation we propose a Fréchet distance-based criterion. Under the assumption of a piecewise constant motion, hysteresis values are computed based on the distance between inspiration and expiration trajectories.

II.A. 4D-CT acquisition

In this study, 4D-CT images were acquired (at 140 kVp, with a tube current of 130–170 mA) using a four-slice fan-beam CT scanner (GE Lightspeed QX/i; GE Heathcare Technologies, Waukesha, WI), and a respiratory surrogate (Real-time Position Management; Varian Medical Systems, Palo Alto, CA). As the patient translates through the scanner, CT images are acquired in cine mode. A complete breathing cycle is acquired at each anatomical position. Cine-mode CT images were acquired at a rate of one image set per 0.4 or 0.5 s, four slices at one time. After the scan is complete, the images are sorted according to the breathing phase assigned by the surrogate. The choice of phase sorting was made according to clinical procedures. Phase sorting is prone to certain kinds of artifacts, especially discontinuities in the appearance when motion amplitude is not regular. Amplitude sorting algorithms are also prone to artifacts. In particular it is not possible to reconstruct all inhale states because sometimes the depths of inhalation are not constant. With breathing periods ranging between 3.7 and 4.3 s, the effective resolution after sorting is approximately 0.4 s. A total of ten respiratory correlated images were generated, numbered 0 through 9. All patients were imaged under light free breathing. A complete description of the process is given in Rietzel *et al.*.[28] We considered 4D-CT scans of five patients treated in radiotherapy for non-small cell lung cancer. The 3D-CT images of the 4D-CT had an in-plane spatial resolution of 512×512, between 88 and 120 slices, and a voxel size of $0.977 \times 0.977 \times 2.5$ mm^3. For all patients, the gross tumor volume (GTV) was manually delineated by an oncologist, with a two-dimensional (2D) slice by slice contouring process, in the end-exhale and end-inhale phases. The contouring variability for the same expert from one image to another

TABLE I. Summary of patient clinical characteristics. GTV motion amplitude has been calculated between the end-exhale and end-inhale states. The first patient had two tumors: (a) in the left lung and (b) in the right lung.

		Tumor-location		GTV	
Patient	Resp. period	Lung	Lobe	Volume (cm^3)	Amplitude (mm)
1	≈4.3 s	(a) left	lower	14.06	7.8
		(b) right	middle	43.58	12
2	≈3.9 s	right	lower	302.0	12.3
3	≈3.7 s	right	lower	203.0	8.2
4	≈4 s	right	middle	24.57	5.0
5	≈4 s	right	middle	18.00	5.9

was comprised between 2% and 9% of the GTV volume of the end-exhale 3D-CT image. Table I depicts the clinical characteristics of the patients.

II.B. Motion estimation

The 4D-CT scans are composed of ten 3D-CT images, numbered from 0 to 9. Image I_5 is the end-exhale image, and I_0 the end-inhale 3D-CT image. I_1, I_2, I_3, I_4 are successive expiration states and I_6, I_7, I_8, I_9 successive inspiration states. The states are cyclic, such that I_0 follows I_9. From n images, there are $n!/(n-2)!$ possible pairwise registrations. Although the deformation fields could be computed for all pairs, we preferred to use fewer registrations to compute the deformation through a free-breathing cycle.

We considered two different methods, denoted by M_1 and M_2, to estimate the motion in a 4D-CT. The first method, M_1, consists in processing deformable registration in both directions between each neighboring pair of 4D-CT states. For example, starting from I_5, we computed $U_{56}, U_{67}, \ldots, U_{45}$, and then we computed $U_{54}, U_{43}, \ldots, U_{65}$. Thus, with M_1 we estimated a set of 20 deformation fields for each 4D-CT data set. The second method, M_2, consists in processing deformable registration between a reference image and all other phases of the 4D-CT scan. Based on the observation that the end-exhale state is the most reproducible state of the free-breathing cycle,[29] we considered I_5 as reference. Thus, with M_2 we computed a set of 18 deformation fields.

From a vector field set a deformation field between any arbitrary 4D-CT states can be generated by composition, denoted by $\circ$. Given two vector fields, U_{XY} and U_{YZ}, the composition is the operation which consists of calculating a new vector field, U_{XZ}, by applying the second vector field, U_{YZ}, to the mapping obtained with the first one: $U_{XZ}=U_{YZ}(U_{XY})$, $U_{XZ}=U_{YZ}\circ U_{XY}$. For example, using the deformation fields computed with M_1, the deformation field U_{52} was calculated as $U_{52}=U_{32}\circ U_{43}\circ U_{54}$. The deformation could also be generated as $U_{52}=U_{12}\circ \ldots \circ U_{67}\circ U_{56}$, but in this method we preferred to use the shortest path.

Figure 1 illustrates the computation of deformable registration with the two methods.

II.C. Evaluation of estimation methods

The method M_1 has the advantage of estimating only small deformations between pairs of images, which can potentially be more accurately computed than large deformations. However, vector fields compositions may induce accumulated errors. The advantage of method M_2 is that any deformation field can be formed from the composition of only two vector fields. We compared M_1 and M_2 for accuracy and consistency in order to decide which method gives a better estimated motion. Accuracy was assessed using control points selected by experts. Consistency was assessed by examining the symmetry and transitivity of vector field compositions.

II.C.1. Control points validation

Today, contrary to rigid registration,[30] deformable registration validation is still an area of active research, and a variety of validation techniques have been proposed (control points, synthetic deformations, vector field operators). Nevertheless, in the absence of a gold standard, this remains a challenging task.

We based our validation on landmark points. For each patient, about 60 landmark points were manually identified by an oncology physician within the lung in the end-inhale

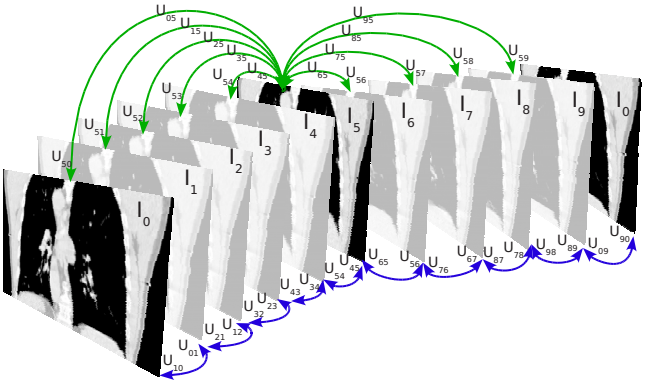

FIG. 1. Deformable registration scheme between images of the 4D-CT. With method M_1, deformation fields are computed between pairs of neighboring images. With M_2 deformation fields are computed between the reference image and each other's image.

image of the 4D-CT. Then, two additional observers identified corresponding landmark points on all other 4D-CT phases. The mean distance between observers' point positions was 2.0 mm with a standard deviation of 1.2 mm. For each landmark and for each phase, a composite reference location was obtained by calculating the mean value of the observer positions. These reference locations were used for vector field validation. They were not used in the registration process.

For each 4D-CT set, vector fields between pairs of images were constructed using both M_1 and M_2. The accuracy of M_1 and M_2 was estimated by computing the target registration error (TRE)[30] which is the distances between the reference landmark locations in the first image and the estimated locations generated using the deformation fields. For example, if U_{XY} is constructed using method M_1, and p_X is a reference location in I_X, its estimate in I_Y is $\mathbf{p}'_Y = \mathbf{p}_X + U_{XY}(\mathbf{p}_X)$. The accuracy of this estimation was determined by computing the distances between $\mathbf{p}'_Y$ and the reference position $\mathbf{p}_Y$. The accuracy for U_{XY} was determined from the mean and SD of these distances over the complete set of landmark points.

II.C.2. Consistency

Deformable registration methods are inherently inconsistent;[31] a deformation field computed from an image I to J does not equal the inverse deformation field, computed from J to I. To overcome this issue, Christensen *et al.*[32] proposed a registration method which jointly estimates the forward and reverse deformation fields by constraining them to be the inverse of one other. In future, it would be interesting to extend such method to 4D-CT images, by constraining the motion fields to be consistent over the breathing cycle with a temporal regularization, for example.

Here, we evaluated the consistency of vector fields generated with M_1 and M_2 as follows. The consistency of a deformation field U_{XY}, is evaluated by computing the mean and SD of the vector norms of composite deformation field $U_{XY} \circ U_{YX}$. In the case of M_1, this results in a variable number of compositions, depending on the distance between X and Y. In the case of M_2, it is usually computed with one (if $Y=5$) or three (if X, $Y \neq 5$) vector fields: $U_{5Y} \circ U_{X5} \circ U_{5X} \circ U_{Y5}$. For each method we estimated the consistency of vector fields computed between successive phases and the consistency of vector fields computed between the reference end-exhale state and all the others. If the two methods were consistent, the composed vector fields would be zero everywhere.

II.D. Lung point trajectories

II.D.1. Building the trajectories

We considered the lung volume points in end-exhale state of the 4D-CT as reference positions for trajectory computation. Point positions through the different states of the 4D-CT could be obtained using the displacements vectors computed M_2. If $\mathbf{p}_5$ is a point in image I_5, its correspondence $\mathbf{p}_Y$ in image I_Y is computed as $\mathbf{p}_Y = \mathbf{p}_5 + U_{5Y}(\mathbf{p}_5)$.

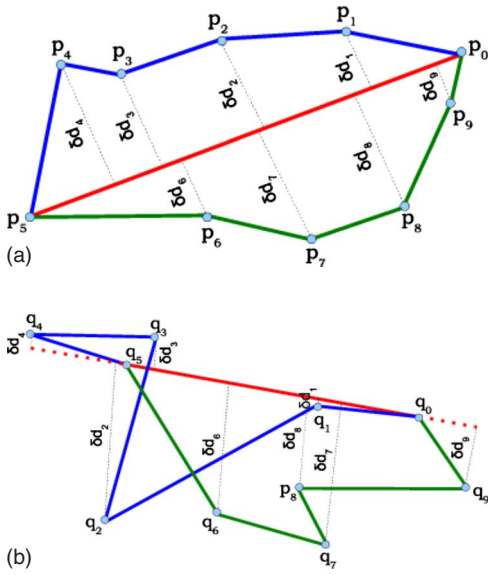

FIG. 2. Two-dimensional illustrations of nonlinearity evaluation for the trajectories of two points ($\mathbf{p}$ and $\mathbf{q}$). The trajectories are built considering the intermediate phases of the 4D-CT over exhalation and inhalation. δ_X denotes the distance between lung point position and the straight line trajectory estimated only between end-exhale and end-inhale phases.

Having the point positions at all breathing states allows to build a complete trajectory. Between successive states we will assume that the trajectory follows a straight line, and that it travels at constant velocity. This assumption is valid if the 4D-CT has sufficient temporal resolution. Thus, the trajectory of a point p, denoted by T_p, is a piecewise linear closed curve in 3D, and is described by T_p: $\Omega_\Phi \rightarrow \mathbb{R}^3$, where Ω_Φ is the set of all possible states. For states $\Phi \in [X, X+1]$ between X and $X+1$, the trajectory is given as

$$T_{\mathbf{p}}(\Phi) = T_{\mathbf{p}}(X) + \lambda_\Phi U_{XX+1}(\mathbf{p}), \tag{1}$$

where $\lambda_\Phi = \Phi - X$, $\lambda_\Phi \in [0,1]$.

II.D.2. Motion nonlinearity

In our previous work,[22] we have made the assumption that points describe a straight line trajectory between end-exhale and end-inhale phases. Here, we evaluate the nonlinearity of the trajectory. For each lung point, at each state X, we computed the distance $\delta_X(\mathbf{p})$, $\delta_X(\mathbf{p}) = d(\mathbf{p}_X, T_L(\mathbf{p}))$ to the straight line trajectory $T_L(p)$. Figure 2 illustrates in 2D the computation of distances to straight line trajectories for two lung points $\mathbf{p}$ and $\mathbf{q}$. We note that due to 2D projection of 3D trajectories, the trajectory of point $\mathbf{q}$ may appear complex and unrealistic.

We evaluated the nonlinearity of the lung point trajectories for six cranio-caudal regions. The cranio-caudal decomposition of the lungs was done as described in Ref. 33. Let H_p be the distance between the lowest and the highest lung points in the cranio-caudal direction. The first region (R_1) is composed of lung points situated between 0% and 10% of

H_p; each of the four (R_2, R_3, R_4, R_5) following regions encompasses 20% of H_p, and the last region (R_6) contains the last 10%.

II.D.3. Motion hysteresis

Previous works[34,35] have studied the hysteresis of 3D tumors motion in patients with lung cancer. The hysteresis was defined as the maximum distance between inhalation and exhalation trajectories. In present study, our purpose was to estimate lung points motion hysteresis from vector fields estimated by deformable registration applied between different phases of the 4D-CT.

The trajectory defined in Eq. (1) is a non-planar polygonal curve. Computing hysteresis between inhalation and exhalation trajectories comes to calculate the maximum distance between inhalation polygonal curve and exhalation polygonal curve. In computational geometry, different metrics are proposed for measuring the distance between two or more polygonal curves: Hausdorff distance[36] and Fréchet distance,[37] for example. A disadvantage of Hausdorff distance is that it does not take into account how points progress along the two trajectories. We used the Fréchet distance, which is well suited to parameterized curves. Each method consists first of considering a set of points describing the two curves, and then computing the distance (usually the Euclidian distance) between each pair of points. Let $L_{exh}(\mathbf{p})$ be the length of a point trajectory $\mathbf{p}$ over exhalation and let $L_{inh}(\mathbf{p})$ be its length over inhalation. Starting from $\mathbf{p}_5$, the point's position in phase 5, we construct a sequence of points along the exhalation trajectory, $\mathbf{p}_{\Phi_1}, \mathbf{p}_{\Phi_2}, \ldots \mathbf{p}_{\Phi_n}$, such that the length between two successive point positions is constant. Then, we construct a similar sequence, starting from $\mathbf{p}_5$ along the inhalation trajectory: $\mathbf{p}_5, \mathbf{p}_{\Psi_1}, \mathbf{p}_{\Psi_2}, \ldots \mathbf{p}_{\Psi_n}$. For Fréchet distance calculation, point positions $\mathbf{p}_{\Phi_{\alpha(t)}}, \mathbf{p}_{\Psi_{\beta(t)}}$ are parameterized as a function of time $\alpha(t)$ and $\beta(t)$, $\alpha(t)$: $[0,1] \rightarrow \{1,2,\ldots,n\}$ and $\beta(t)$: $[0,1] \rightarrow \{1,2,\ldots,m\}$. Finding the Fréchet distance $D_F(\mathbf{p})$ requires finding the parameterization of functions $\alpha(t)$ and $\beta(t)$ that minimize the maximum distance between inhalation and exhalation trajectories of the point $\mathbf{p}$ as indicated by

$$D_F(\mathbf{p}) = \min_{\alpha(t),\beta(t)} \{ \max_{t \in [0,1]} d(\mathbf{p}_{\Phi_{\alpha(t)}}, \mathbf{p}_{\Psi_{\beta(t)}}) \}, \quad (2)$$

where $d(\mathbf{p}_{\Phi_{\alpha(t)}}, \mathbf{p}_{\Psi_{\beta(t)}})$ denotes the Euclidian distance between points $\mathbf{p}_{\Phi_{\alpha(t)}}$ and $\mathbf{p}_{\Psi_{\beta(t)}}$.

We assume that point motion is uniform over exhalation and inhalation, namely that $\alpha(t) = \beta(t) = k$, which simplifies the measurement of the Fréchet. This simplified Fréchet distance is used to compute trajectory hysteresis, using the maximum distance between pairs of points $(\mathbf{p}_{\Phi_k}, \mathbf{p}_{\Psi_k})$ as follows:

$$Hyst_{\mathbf{p}} \approx \max_{k=1..n} d(\mathbf{p}_{\Phi_k}, \mathbf{p}_{\Psi_k}). \quad (3)$$

We used the same number n ($n=100$ in our experiments), to describe inhalation and exhalation curves. Figure 3 illustrates in 2D the hysteresis computation for two point trajectories with $n=9$.

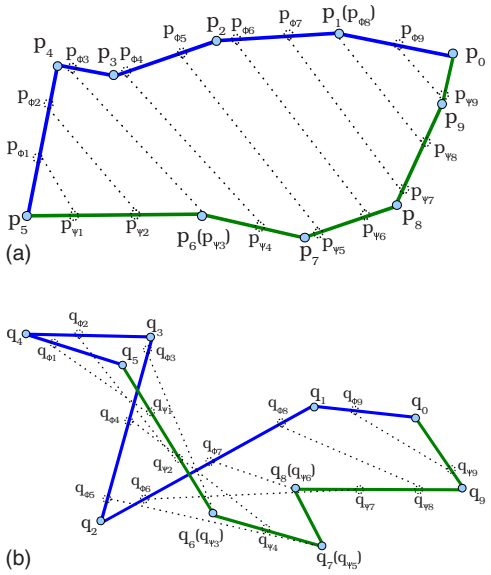

FIG. 3. Illustration of hysteresis computation for two different lung points ($\mathbf{p}$ and $\mathbf{q}$) starting from state 5 point position and considering a sequence of nine equal distant points positions ($\mathbf{p}_{\Phi_1}, \ldots, \mathbf{p}_{\Phi_9}$, respectively, $\mathbf{q}_{\Phi_1}, \ldots, \mathbf{q}_{\Phi_9}$) over exhalation trajectory and nine equal distant points ($\mathbf{p}_{\Psi_1}, \ldots, \mathbf{p}_{\Psi_9}$, respectively, $\mathbf{q}_{\Psi_1}, \ldots, \mathbf{q}_{\Psi_9}$) over inhalation trajectory. For point $\mathbf{p}$, hysteresis is well estimated with the metrics we used while it is overestimated for point $\mathbf{q}$. For better visualization the illustrations are presented in 2D.

We used the six cranio-caudal regions (see Sec. II D 2) decomposition for lung point hysteresis evaluation.

III. RESULTS

Results are classified in four sections. Section III A presents accuracy and consistency results for the two motion estimation methods. Section III B presents nonlinearity results, Sec. III C hysteresis results. All these results were calculated for lung points, with GTV points not included. GTV motion results are summarized in Sec. III D.

III.A. Accuracy and consistency of estimation methods

Table II summarizes the mean (μ) and SD (σ) values for accuracy and consistency. The column "Amplitude" indicates the average motion amplitude between end-exhale and end-inhale states. The last two columns of Table II report student t-test of comparisons between the two deformation field estimation methods (M_1 and M_2) for accuracy and consistency. "=" denotes that the two methods were not significantly different. "+" denotes that the two methods were significantly different (p values are given). A 5% confidence level was adopted.

III.B. Motion nonlinearity

We computed the nonlinearity value of each lung point at each 4D-CT phase of exhalation and inhalation. Figure 4 summarizes, for each patient, the average lung point trajec-

TABLE II. Summary of accuracy and consistency results, and differences between the two deformation field estimation methods. μ denotes the mean and σ the standard deviation.

Patient	Amplitude $\mu(\sigma)$ (mm)	Accuracy $\mu(\sigma)$ (mm)		Consistency $\mu(\sigma)$ (mm)		Difference $\mathbf{M_1}$,$\mathbf{M_2}$ (p value)	
		M_1	M_2	M_1	M_2	Accuracy	Consistency
1	5.2(2.6)	2.3(1.3)	2.1(1.3)	0.8(1.1)	0.8(1.1)	+(0.07)	=(0.97)
2	6.7(4.2)	3.2(2.2)	2.9(2.2)	1.1(1.3)	1.2(1.5)	=(0.41)	=(0.47)
3	5.1(3.7)	2.2(1.2)	1.9(1.2)	0.7(0.9)	0.8(1.0)	=(0.95)	=(0.68)
4	5.6(3.1)	2.1(1.5)	2.1(1.5)	0.9(1.3)	1.0(1.3)	=(0.98)	=(0.60)
5	5.4(3.1)	2.7(2.0)	2.4(1.8)	0.9(1.5)	1.0(1.6)	=(0.51)	=(0.52)

tory nonlinearity values over exhalation in the top graphic chart (a) and over inhalation in the second graphic chart (b). In the graphic charts, the height of each vertical bar is the region average nonlinearity at the corresponding exhalation or inhalation phase. Nonlinearity could not be estimated for region R_1 of patient 2 because this part was missing from the 4D-CT acquisition. The patient data available for this study had a 2.5 mm interslice distance. An interesting point was to evaluate the percentage of lung volume points with a nonlinearity greater than 2.5 mm. Values below 2.5 mm may be considered within image voxel tolerance, and for points with such values, trajectories can be approximated with a straight line between end exhale and end inhale. Percentages of lung volume points with trajectory nonlinearity values greater than the 2.5 mm slice thickness were comprised between 0.68% and 19.67% during the exhalation phase, and between 2.25% and 29.61% during the inhalation phase. Table III depicts the percentage of lung volume with a motion nonlinearity superior to 2.5 mm at each 4D-CT state for each patient.

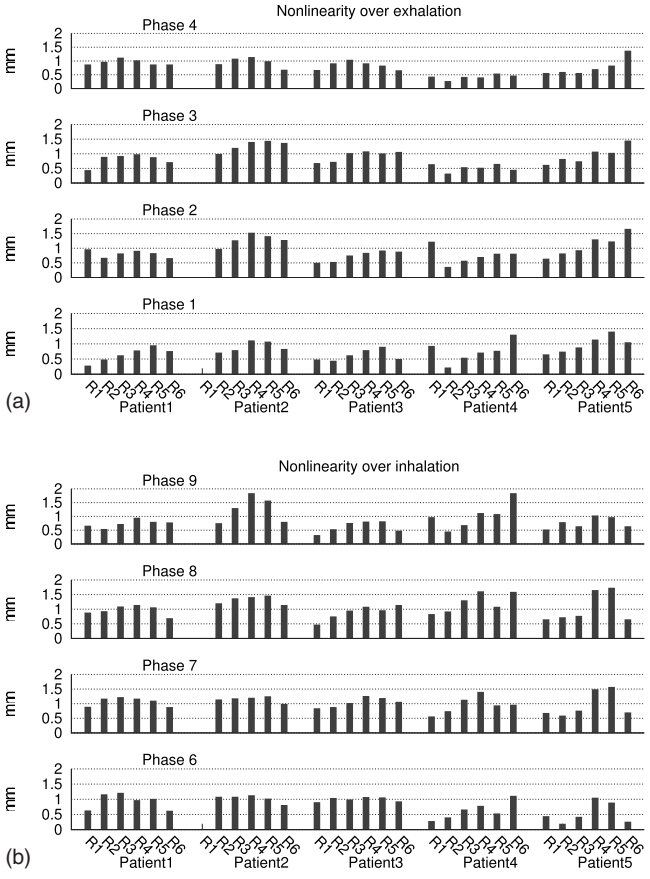

FIG. 4. Summary of average point trajectory nonlinearity values for each patient cranio-caudal region (denoted by R_1, R_2, R_3, R_4, R_5, and R_6) at each 4D-CT exhalation phase in the top graphic chart (a), and at each inhalation phase in the second graphic chart (b).

In Table IV the maximum nonlinearity values for each region are presented.

Figure 5 illustrates a map of the maximum nonlinearity values for exhalation and for inhalation on transversal, cranio-caudal and sagittal left lung slices of patient 2. As indicated by the gray scale, high intensities correspond to high nonlinearity values (a maximum of 9.4 mm for this patient) and low intensities to smaller values (0 mm is the minimum value). We can note the high nonlinearity values in the second, third and fourth 20% regions in the cranio-caudal direction.

III.C. Motion hysteresis

Figure 6 illustrates trajectory lengths over exhalation and over inhalation, hysteresis and the ratio between hysteresis and trajectory length. In the two upper charts, we represented the average trajectory length region by region for the exhalation (left image) and inhalation phase (right image). The left down graphic chart illustrates the average hysteresis values, and the right down graphic chart illustrates the average ratio between trajectory length and hysteresis.

Table V depicts the maximum hysteresis (in millimeters) for each region.

III.D. GTV motion

A specific region of interest in the lung is the tumor site. We evaluated the mean and the maximum values of nonlinearity and hysteresis of points within the GTV. We also computed the average trajectory lengths over exhalation and inhalation. Results for these measures are summarized in Table VI. For comparison purposes with previous study[34] the table

TABLE III. Percentages of lung volume points with nonlinearity greater than 2.5 mm at each 4D-CT phase. Last two rows depict the total percentage of lung volume points with nonlinearity motion superior to 2.5 mm over exhalation and over inhalation.

%	Patient 1	Patient 2	Patient 3	Patient 4	Patient 5
Phase 0 (end inhale)	0.00	0.00	0.00	0.00	0.00
Phase 1	0.58	2.99	0.64	0.46	3.78
Phase 2	0.09	8.99	0.30	0.21	9.45
Phase 3	0.01	6.57	0.44	0.18	6.66
Phase 4	0.00	1.11	0.00	0.08	1.13
Phase 5 (end exhale)	0.00	0.00	0.00	0.00	0.00
Phase 6	0.08	0.35	0.08	0.75	1.62
Phase 7	0.13	1.15	1.76	4.61	11.27
Phase 8	1.42	4.33	0.56	7.67	13.90
Phase 9	0.61	11.37	0.25	3.13	2.82
Exhalation	0.64	13.67	1.23	0.79	8.48
Inhalation	2.15	14.80	2.43	11.20	16.92

depicts the hysteresis values in 3D and for the three planes: cranio-caudal (*CC*), sagittal (*SG*) and trans-axial (*TA*).

IV. DISCUSSION

IV.A. Evaluation of estimation methods

We studied two patient specific motion estimation methods, M_1 and M_2, from 4D-CT data. Although M_1 requires computation of 20 deformation fields, while M_2 requires only 18, computation times were similar: about 2.5 h on a PC Pentium 4 (3.2 GHz, 2 GiB Ram). Convergence is reached faster with method M1 because the deformations between successive phases are smaller. Approximately 20–50 iterations of deformable registration were needed for one vector field estimation with method M_1, while with M_2, the end-inhale to end-exhale vector field required about 250 iterations.

We evaluated the accuracy and the consistency and found that differences between M_1 and M_2 were not significant; the values of the mean and standard deviation were similar. For consistency, this similarity may be due to the fact that we proceeded with a global evaluation. It does not mean that locally, the two methods are always similar. This point needs further investigation, and a gold-standard validation method for deformable registration. The accuracy results of the two methods were not significantly different except for patient 1. This patient had two tumors, one in the left lung and the other in the right lung. This fact could imply different behaviors inside lung, which can lead to differences between the two methods. Mean values of accuracy were on the order of the image resolution and comparable to inter-observer variability (1.9 mm), with slightly better results for M_2: 2.3 mm versus 2.5 mm.

IV.B. Trajectories

The parameter λ_Φ in Eq. (1) models the motion between successive 4D-CT breathing phases which we supposed to be uniform, and the trajectory described by a point in a straight line. The parameter λ_Φ could be related to a breathing model cycle such as the one proposed by Lujan *et al.*[4] by scaling the time, or to the tidal volume and its temporal derivative in the five-dimensional model proposed by Low *et al.*[7] allowing to model different respiration behaviors. As mentioned in Ref. 7, however, the breathing motion is very complex and is not well modeled as a simple function of time. Ideally, a priori patient specific physiological information would be needed to simulate the temporal behavior of point trajectories during breathing. Under the assumption that the thorax motion is smooth during free breathing, points in subsequent image volumes could also be connected with spline functions. However, the temporal resolution is relatively low, and a quadratic or cubic spline may over fit. The computation time would also be more important. Seppenwoolde *et al.*[34] ap-

TABLE IV. For each patient (denoted by P1, P2, P3, P4, P5) the table depicts the maximum nonlinearity values in each region cranio-caudal region.

	Exhalation					Inhalation				
Max(mm)	P1	P2	P3	P4	P5	P1	P2	P3	P4	P5
$\mathbf{R_1}$	1.8	—	2.2	2.9	2.3	1.8	—	2.1	4.2	1.5
$\mathbf{R_2}$	2.1	3.3	2.5	1.9	3.2	2.7	2.9	3.0	3.1	3.2
$\mathbf{R_3}$	3.7	6.3	3.1	3.3	4.9	3.9	8.3	3.5	3.8	4.2
$\mathbf{R_4}$	3.5	8.2	4.2	4.4	7.3	4.3	9.4	5.6	6.6	8.3
$\mathbf{R_5}$	4.5	6.8	4.3	3.9	9.6	4.0	6.4	3.7	5.2	6.7
$\mathbf{R_6}$	1.9	4.9	5.1	6.4	7.2	3.1	4.5	2.6	7.8	4.2

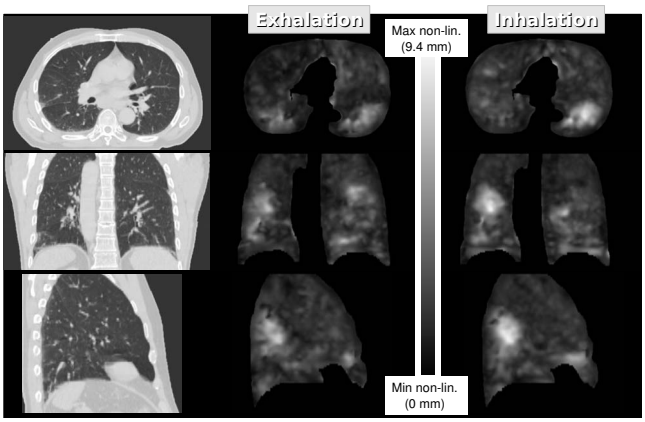

FIG. 5. Illustration of trajectory nonlinearity values on a transversal, coronal and sagittal slice for patient 2.

proximated the inhalation and exhalation trajectories with a sinusoidal function with varying asymmetry. Another alternative solution would be to use a 4D-CT composed of sufficient 3D-CT phases, allowing a very good approximation of the real movement inside the lung. The disadvantage of this solution is that for large breathing amplitudes, additional 3D-CT images would be needed resulting in higher dose to the patient.

IV.C. Motion nonlinearity

Analysis of the nonlinearity data suggests that the upper lung has nearly linear motion, while the motion in the lower-middle regions is less linear (see Table IV). The trajectory lengths also increased in the lower parts of the lung (see Fig. 6), which suggests that nonlinearity is correlated with trajectory length. Trajectory lengths were greater over inhalation than over exhalation, but the difference was not statistically significant ($p=0.19$). The 4D-CT data used in this study were acquired from five patients presenting a diaphragmatic respiration. In the future, it would be interesting to analyze the data of patients with a thoracic respiration.

The majority of the lung (83.1%–97.9%) and GTV volume points (91.8%–99.9%) had a motion nonlinearity below 2.5 mm inter-slice distance. This suggests that for a scanner acquisition with a slice thickness of 2.5 mm, these points trajectories could be approximated with a straight line trajectory over inhalation and over exhalation. The straight line approximation based on nonlinearity ensures the fact that along the entire free-breathing trajectory, the distance between the detailed trajectory and the straight line trajectory is

TABLE V. The maximum hysteresis values for each cranio-caudal region of each patient.

Max(mm)	Patient 1	Patient 2	Patient 3	Patient 4	Patient 5
R_1	2.3	⋯	2.4	4.8	4.9
R_2	4.4	6.1	4.0	3.8	5.6
R_3	4.9	9.1	5.7	6.6	9.1
R_4	6.7	10.4	5.9	7.8	9.7
R_5	6.5	10.6	7.1	10.7	13.7
R_6	3.9	5.5	5.7	7.9	13.9

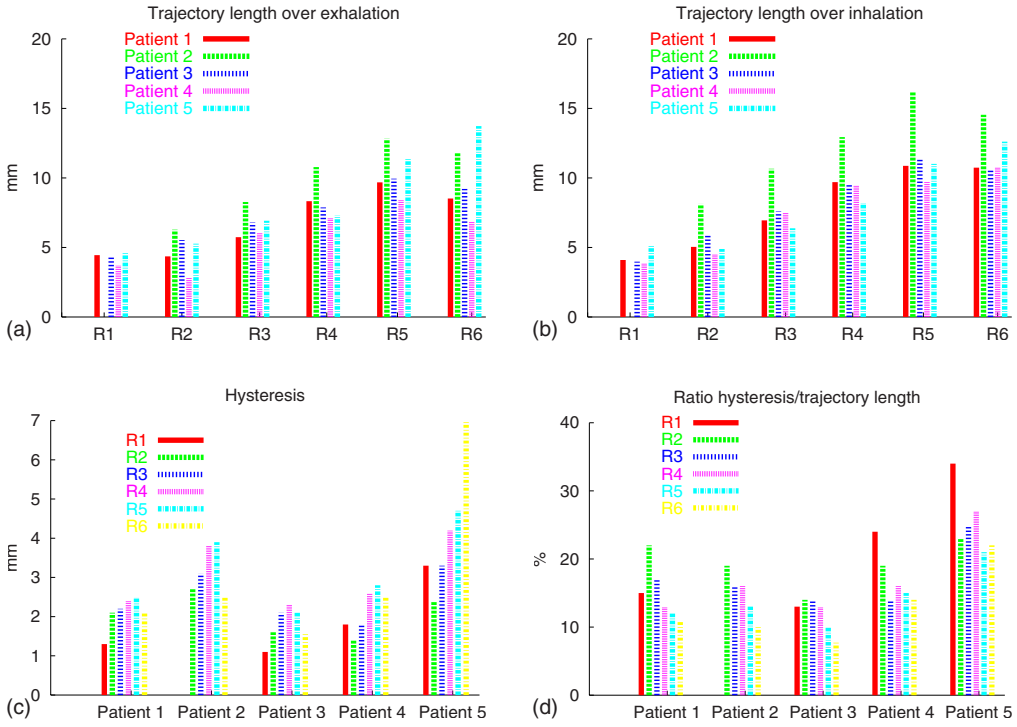

FIG. 6. Illustration of average trajectory lengths, hysteresis and ratio between hysteresis and trajectory length for each cranio-caudal region of each patient. Bars correspond to average trajectory length values over exhalation (upper left chart) or over inhalation (upper right chart), to average hysteresis values (left down chart), and to average values of the ratio between hysteresis and trajectory length (right down chart).

TABLE VI. Summary of trajectory lengths and nonlinearity over exhalation and over inhalation of hysteresis values for patients' GTVs. The (a) row of patient 1 contains values calculated for the left lung tumor, and the (b) row contains values for the right lung tumor. *CC* denotes the coronal plane, *SG* the sagittal plane and *TA* the transaxial plane.

	Exhalation (mm)			Inhalation (mm)			Hysteresis (mm)				
		Nonlin			Nonlin		μ				
	L_{exh}	μ	Max	L_{inh}	μ	Max	CC	SG	TA	3D	Max
$\mathbf{P_1}$ (a)	10.5	1.7	3.5	9.8	2.0	3.9	4.2	2.0	1.5	4.8	7.5
(b)	13.1	1.2	2.7	14.1	1.5	2.8	1.2	0.8	1.7	2.1	3.9
$\mathbf{P_2}$	14.6	1.8	5.2	17.6	2.1	4.9	3.4	1.4	3.2	4.6	9.4
$\mathbf{P_3}$	9.8	1.4	3.9	11.5	1.5	4.8	1.7	1.6	1.0	2.4	5.6
$\mathbf{P_4}$	7.0	1.2	4.0	10.7	2.2	5.5	2.5	0.9	2.4	3.5	7.3
$\mathbf{P_5}$	7.0	0.7	2.1	13.6	2.3	4.0	5.6	2.1	2.2	6.1	9.7

always inferior to 2.5 mm if the exhalation and inhalation trajectories are considered separately. The nonlinearity information could be integrated in a motion model construction, and the model could be simplified for regions where the nonlinearity is within image voxel tolerance. Three patients (1, 3, and 4) had a very small percentage of points with motion nonlinearity greater than 2.5 mm, while two patients (2 and 5) exhibited more nonlinearity. The first group had significantly different nonlinearity values between exhalation and inhalation (p-values 0.04/0.1/0.001), while the second group did not (p-values 0.34/0.25). All patients presented larger lung and GTV motion nonlinearity over inhalation than over exhalation. Pooled data analysis of the five patients showed a very highly significant difference between inhalation and exhalation ($p=0.001$) nonlinearity, most with lower values over exhalation. Furthermore, in all patients, the highest nonlinearity was found in the lower-middle regions of the lungs. These results are consistent with a respiration process which involves different exhalation and inhalation mechanisms: exhalation is a passive, smooth process, during which the diaphragm and the respiration muscles relax, while inspiration is a complex active, less linear process, with diaphragm and respiration muscles inducing different constraints in lung.

IV.D. Motion hysteresis

For motion hysteresis, we observed relatively large hysteresis for the lower-middle regions in all patients. We noticed that longer trajectory lengths may be associated with greater motion hysteresis. In addition, the upper-middle regions of the lung present small hysteresis, but a large ratio between hysteresis and trajectory length which suggests that in the upper regions of the lung the motion is more subject to hysteresis than in the lower regions. For areas within the GTV volume, hysteresis was seen with smaller motion amplitudes too. For all GTVs, except patient 1(b) right lung tumor, larger hysteresis values were seen in the coronal plane, and variations were seen in sagittal and transaxial: patients 1(a) and 3 presented larger sagittal values, and patients 2,4, and 5 larger trans-axial values. These observations are close to those presented in previous studies.[34,35]

We can note with Eq. (3) that hysteresis is overestimated for some trajectory shapes. An exact hysteresis value could be computed if point velocity was known for exhalation and inhalation. This would allow to calculate the functions of time $\alpha(t)$ and $\beta(t)$ for the Fréchet distance formula 2. $\alpha(t)$ and $\beta(t)$ could be calculated from scaling acquisition times. By taking into account the acquisition time, we could observe if the velocities are uniform or not over the inhalation and exhalation phases. Moreover, by using a respiration model (for example the one proposed by Lujan *et al.*[4]), it would be possible to modelize the point trajectories for different breathing behaviors and to analyze hysteresis variations.

IV.E. Method limitations

Intensity based deformable registration methods are dependent on image quality, and also on image resolution. Image artifacts may induce errors. In this case, trajectories would be estimated with erroneous intensity differences, and they would not reveal the real lung motion. For patient 2 we observed important nonlinearity values for regions 2, 3, and 4. Visual inspection of the image I_9 revealed a blur offset artifact of about 2 mm in the transversal plane in these image regions. This may explain the number of points with a nonlinearity superior to 2.5 mm in these regions for patient 2. The blur offset artifact is illustrated in Fig. 7. The left image shows an artifact in the axial slice of I_9, while the right image shows a blur-free slice from end-exhale image I_5. This

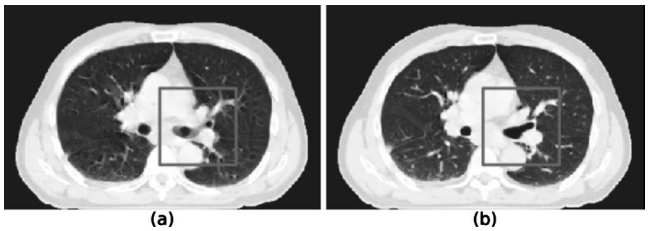

FIG. 7. Left image (a)—illustration of blur-offset artifact on an axial slice of image I_9 for patient 2. Right image (b)—a blur artifact-free axial slice of image I_5.

may explain the high degree of nonlinearity in these regions for patient 2. In addition, the 4D-CT of patients with irregular breathing present artifacts that interfere with motion estimation. Improvement of 4D imaging is an area of continued study.

Landmark based validation is difficult and time consuming even for experts. In homogenous regions no landmarks can be identified, which limits its applicability. However, by choosing a large number of points, and distributing their arrangement throughout both lungs, we have mitigated this problem. With an inter-expert variability of point identification of 2 mm, and image inter-slice resolution of 2.5 mm, accuracy of 2.3 mm was judged acceptable by oncologists.

V. CONCLUSION

In this study, we introduced and compared two methods for patient specific motion estimation allowing to follow lung and tumor displacements and deformations during free breathing. In addition, we proposed techniques to automatically extract physiological parameters of lung motion. Results demonstrate that lung motion during free breathing is prone to nonlinearity and hysteresis, and that these physiological effects vary across different regions within the lung. Even if we identified some characteristics common to all patients, we do not pretend to extract general characteristics of lung motion behavior, but provide tools for patient specific motion analysis. In the future, the physiological information may be integrated to build a general 4D thorax atlas, with different clinical applications. In radiotherapy, for example, it could be useful for dosimetry studies, and for online image guidance procedures. It could also allow interpatient comparisons for population studies aimed at extracting common and specific respiratory traits.

[a]Author to whom correspondence should be addressed; Electronic mail: vboldea@gmail.com
[b]Present address: Department of Radiation Oncology, University of California, San Diego, La Jolla, California 92093-0893

[1]M. van Herk, "Errors and margins in radiotherapy," Semin. Radiat. Oncol. **14**(1), 52–64 (2004).
[2]A. Trofimov, E. Rietzel, H. M. Lu, B. Martin, S. B. Jiang, G. T. Y. Chen, and T. Bortfeld, "Temporo-spatial imrt optimization: Concepts, implementation and initial results," Phys. Med. Biol. **50**(12), 2779–2798 (2005).
[3]P. J. Keall, S. Joshi, S. S. Vedam, J. V. Siebers, V. R. Kini, and R. Mohan, "Four-dimensional radiotherapy planning for DMLC-based respiratory motion tracking," Med. Phys. **32**(4), 942–951 (2005).
[4]A. E. Lujan, J. M. Balter, and R. K. Ten Haken, "A method for incorporating organ motion due to breathing into 3D dose calculations," Med. Phys. **26**(5), 715–720 (1999).
[5]T. Neicu, H. Shirato, Y. Seppenwoolde, and S. B. Jiang, "Synchronized moving aperture radiation therapy (SMART): Average tumor trajectory for lung patients," Phys. Med. Biol. **48**(5), 587–598 (2003).
[6]H. Wu, G. C. Sharp, B. Salzberg, D. Kaeli, H. Shirato, and S. B. Jiang, "A finite state model for respiratory motion analysis in image guided radiation therapy," Phys. Med. Biol. **49**(23), 5357–5372 (2004).
[7]D. A. Low, P. J. Parikh, W. Lu, J. F. Dempsey, S. H. Wahab, J. P. Hubenschmidt, M. M. Nystrom, M. Handoko, and J. D. Bradley, "Novel breathing motion model for radiotherapy," Int. J. Radiat. Oncol., Biol., Phys. **63**(3), 921–929 (2005).
[8]P. Keall, "Four-dimensional computed tomography imaging and treatment planning," Semin. Radiat. Oncol. **14**(1), 81–90 (2004).
[9]B. A. Simon, G. E. Christensen, D. A. Low, and J. M. Reinhardt, "Computed tomography studies of lung mechanics," Proc. Am. Thorac. Soc. **2**(6), 506–507 (2005); **2**(6), 517–521 (2005).
[10]K. K. Brock, M. B. Sharpe, L. A. Dawson, S. M. Kim, and D. A. Jaffray, "Accuracy of finite element model-based multi-organ deformable image registration," Med. Phys. **32**(6), 1647–1659 (2005).
[11]T. A. Sundaram and J. C. Gee, "Towards a model of lung biomechanics: Pulmonary kinematics via registration of serial lung images," Med. Image Anal. **9**(6), 524–537 (2005).
[12]J. M. Blackall, S. Ahmad, M. E. Miquel, J. R. McClelland, D. B. Landau, and D. J. Hawkes, "MRI-based measurements of respiratory motion variability and assessment of imaging strategies for radiotherapy planning," Phys. Med. Biol. **51**(17), 4147–4169 (2006).
[13]E. A. Hoffman and D. Chon, "Computed tomography studies of lung ventilation and perfusion," Proc. Am. Thorac. Soc. **2**(6), 492–498 (2005); **2**(6), 506 (2005);
[14]W. A. Kalender, "X-ray computed tomography," Phys. Med. Biol. **51**(13), R29–43 (2006).
[15]M. Defrise and G. T. Gullberg, "Image reconstruction," Phys. Med. Biol. **51**(13), R139–154 (2006).
[16]D. Sarrut, "Deformable registration for image-guided radiation therapy," Z. Med. Phys. **16**(4), 285–297 (2006).
[17]I. Sluimer, A. Schilham, M. Prokop, and B. van Ginneken, "Computer analysis of computed tomography scans of the lung: A survey," IEEE Trans. Med. Imaging **25**(4), 385–405 (2006).
[18]M. Foskey, B. Davis, L. Goyal, S. Chang, E. Chaney, N. Strehl, S. Tomei, J. Rosenman, and S. Joshi, "Large deformation three-dimensional image registration in image-guided radiation therapy," Phys. Med. Biol. **50**, 24 (2005).
[19]J. B. A. Maintz and M. A. Viergever, "A survey of medical image registration," Med. Image Anal. **2**(1), 1–36 (1998).
[20]H. Lester and S. R. Arridge, "A survey of hierarchical non-linear medical image registration," Pattern Recogn. **32**(1), 129–149 (1999).
[21]J. Modersitzki, *Numerical Methods for Image Registration*, Numerical Mathematics and Scientific-Computation (Oxford University Press, NY, 2004).
[22]D. Sarrut, V. Boldea, S. Miguet, and C. Ginestet, "Simulation of 4D CT images from deformable registration between inhale and exhale breathhold CT scans," Med. Phys. **33**(3), 605–617 (2006).
[23]J. P. Thirion, "Image matching as a diffusion process: An analogy with Maxwell's demons," Med. Image Anal. **2**(3), 243–260 (1998).
[24]X. Pennec, P. Cachier, and N. Ayache, "Understanding the demon's algorithm: 3D non rigid registration by gradient descent," in *MICCAI 1999*, edited by C. Taylor and A. Colschester, LNCS (Springer-Verlag, London, 1999), Vol. 1679, pp. 597–605.
[25]K. E. Sixel, M. Ruschin, R. Tirona, and P. C. F. Cheung, "Digital fluoroscopy to quantify lung tumor motion: Potential for patient-specific planning target volumes," Int. J. Radiat. Oncol., Biol., Phys. **57**(3), 717–723 (2003).
[26]G. D. Hugo, D. Yan, and J. Liang, "Population and patient-specific target margins for 4D adaptive radiotherapy to account for intra- and inter-fraction variation in lung tumor position," Phys. Med. Biol. **52**(1), 257–274 (2007).
[27]T. Guerrero, K. Sanders, E. Castillo, Y. Zhang, L. Bidaut, T. Pan, and R. Komaki, "Dynamic ventilation imaging from four-dimensional computed tomography," Phys. Med. Biol. **51**, 777–791 (2006).
[28]E. Rietzel, T. Pan, and G. T. Y. Chen, "Four-dimensional computed tomography: Image formation and clinical protocol," Med. Phys. **32**(4), 874–889 (2005).
[29]G. S. Mageras and E. Yorke, "Deep inspiration breath hold and respiratory gating strategies for reducing organ motion in radiation treatment," Semin. Radiat. Oncol. **14**(1), 65–75 (2004).
[30]J. West *et al.*, "Comparison and evaluation of retrospective intermodality brain image registration techniques," J. Comput. Assist. Tomogr., **21**(4), 554–566 (1997).
[31]X. Pennec, C. R. G. Guttmann, and J. P. Thirion, "Feature-based registration of medical images: Estimation and validation of the pose accuracy," *MICCAI 1998*, LNCS (Springer-Verlag, London, 1998), Vol. 1496, pp. 1107–1114.
[32]G. E. Christensen and H. J. Johnson, "Consistent image registration," IEEE Trans. Med. Imaging **20**(7), 568–582 (2001).
[33]V. M. Remouchamps, N. Letts, D. Yan, F. A. Vicini, M. Moreau, J. A. Zielinski, J. Liang, L. L. Kestin, A. A. Martinez, and J. W. Wong, "Three-dimensional evaluation of intra- and interfraction immobilization of lung and chest wall using active breathing control: A reproducibility study with

breast cancer patients," Int. J. Radiat. Oncol., Biol., Phys. **57**(4), 968–978 (2003).
[34]Y. Seppenwoolde, H. Shirato, K. Kitamura, S. Shimizu, M. van Herk, and J. V. Lebesque, "Precise and real-time measurement of 3D tumor motion in lung due to breathing and heartbeat, measured during radiotherapy," Int. J. Radiat. Oncol., Biol., Phys. **53**(4), 822–834 (2002).
[35]G. S. Mageras, A. Pevsner, E. D. Yorke, K. E. Rosenzweig, E. C. Ford, A. Hertanto, S. M. Larson, D. M. Lovelock, Y. E. Erdi, S. A. Nehmeh, J. L. Humm, and C. C. Ling, "Measurement of lung tumor motion using respiration-correlated CT," Int. J. Radiat. Oncol., Biol., Phys. **60**(3), 933–941 (2005).
[36]G. Rote, "Computing the minimum Hausdorff distance between two point sets on a line under translation," Inf. Process. Lett. **38**(3), 123–127 (1991).
[37]H. Alt and M. Godau, "Computing the Fréchet distance between two polygonal curves," Int. J. Comput. Geom. Appl. **5**(1–2), 75–91 (1995).